NANO LETTERS

Communication

Revealing the correlation between catalytic selectivity and the local coordination environment of Pt single atom

Yong Xu, Mingyu Chu, Fangfang Liu, Xuchun Wang, Yu Liu, Muhan Cao, Jin Gong, Jun Luo, Haiping Lin, Youyong Li, and Qiao Zhang

Nano Lett., **Just Accepted Manuscript** • DOI: 10.1021/acs.nanolett.0c02940 • Publication Date (Web): 10 Aug 2020

is published by the American Chemical Society. 1155 Sixteenth Street N.W., Washington, DC 20036

Revealing the correlation between catalytic selectivity and the local coordination environment of Pt single atom

Yong Xu,[1,2,†] Mingyu Chu,[2,†] Fangfang Liu,[2,†] Xuchun Wang,[2,†] Yu Liu,[2] Muhan Cao,[2] Jin Gong,[2] Jun Luo,[3] Haiping Lin [2,] Youyong Li,[2] Qiao Zhang[2,*]*

[1]Guangzhou Key Laboratory of Low-Dimensional Materials and Energy Storage Devices, Collaborative Innovation Center of Advanced Energy Materials, School of Materials and Energy, Guangdong University of Technology, Guangzhou, 510006, Guangdong, China

[2]Institute of Functional Nano & Soft Materials (FUNSOM), Jiangsu Key Laboratory for Carbon-Based Functional Materials and Devices, Soochow University, Jiangsu, 215123, China

[3]Institute for New Energy Materials and Low-Carbon Technologies, School of Materials Science and Engineering, Tianjin University of Technology, Tianjin 300384, China

Keywords: Local coordination environment; single atom catalyst; catalytic selectivity; Pt; propyne semi-hydrogenation.

ABSTRACT: Single atom catalysts (SACs) have recently attracted great attention in heterogeneous catalysis and been regarded as ideal models for investigating the strong interaction between metal and support. Despite the huge progress over the past decade, the deep understanding

on the structure-performance correlation of SACs at a single atom level still remains great challenges. In this study, we demonstrate that the variation in the coordination number of Pt single atom can significantly promote the propylene selectivity during propyne semi-hydrogenation (PSH) for the first time. Specifically, the propylene selectivity greatly increases from 65.4% to 94.1% as the coordination number of Pt–O increased from ~3.4 to ~5, whereas the variation in the coordination number of Pt–O slightly influences the turnover frequency (TOF) values of SACs. We anticipate that the present work may deepen the understanding on the structure-performance of SACs and also promote the fundamental researches in single atom catalysis.

Introduction

Single atom catalysts (SACs) have recently emerged as a new frontier in heterogeneous catalysis owing to their unique propertie including maximized utility of metals, low-coordination environment and strong metal-support interactions.[1-7] Since the pioneering work from Zhang *et al.* in 2011,[8] SACs have been widely used to catalyze vairous reactions, including CO oxidation,[8-12] CH_4 conversion,[13,14] CO_2 reduction,[15-18] hydrogen evolution reaction,[19,20] water gas shift reaction,[21,22] hydrogenation,[23-26] *etc*. Many strategies have been developed to synthesize SACs over the last decade, and the familiy of SACs has been expanded from noble metals (Pt, Pd, Rh, *etc.*) to non-noble metals (Co, Fe, Ni, *etc.*).[18,27-34] With the in-depth research, chemists realize the enhancement of activity and selectivity on SACs may be attributed to the signifcantly different electronic properties of the isolated metal atoms in SACs. As a result, trenmendous effort has been devoted to undestanding the correlation between the structure of single atom and catalytic performace.

It has recently been reported that the activity of SACs is strongly determined by the local coordination environment (*e.g.*, coordination atom and number) of each isolated atom. For

example, Co–N_4 SAC displayed much higher activity than Co–$N_{4-x}C_x$ SAC toward CO_2 electrocatalytic reduction (CO_2RR) because Co–N_4 was found to promote the kinetics of CO_2 activation.[35] Gong *et al.* reported that Ni–N_2–C_2 SAC exhibited higher activity and selectivity than Ni–N_3–C_1 and Ni–N_4–C_1 for CO_2RR.[36] Fei *et al.* claimed that Ni–N–C SAC exhibited dramatically enhanced oxygen evolution reaction activity (OER).[37] In another case, Zhang *et al.* demonstrated that doping Fe SACs with S (Fe–N_4–S_2) significantly promoted the activity of oxygen reduction reactions (ORR).[38] On the other hand, the obtained catalytic performance on SACs may obviously different with the changes in coordination number. Jakub and coworkers claimed that the CO adsorption on Ir/Fe_3O_4 SACs was much stronger than that on Ir nanoparticles.[39] Similarly, Wang *et al.* revealed that Co-SACs exhibited a promising activity towards CO_2RR when the Co–N coordination number was decreased from 4 to 2.[40] Ren *et al.* indicated that the increase in Pt–O coordination number (from ~2 to ~4) of Pt/FeO_x SACs resulted in a significant improvement in the activity of CO oxidation.[41] However, previous reports mainly focus on studying the synergy between coordination environment and activity, while the the correlation of coordination environment and SACs' selectivity has not been systematically investigated yet. The great challenges in the regulation of coordiantion enviroment in SACs, especially in oxide-supported SACs, have seriously impeded their application in catalysis.[41]

Benefitting from the strong adsorption of reactants, noble metal atoms are generally recognized as promising sites for many reactions, however, they suffer the disadvantage of poor selectivity.[14,24,41] The precise control on the selectivity of SACs is therefore of tremendous significance. Given that the geometric isolation of metal atoms in SACs exihibits promising selectivity for hydrogenation owing to their variable adsorption abilities for reactants, intermediates and products,[14,24,41] we beleive that the control on the coordination number of single

atom in SACs can correspondingly tailor the selectivity of different products. Herein, we systematically investigated the correlation between coordination number and selectivity in propyne semi-hydrogenation (PSH) over Pt/FeO_xH_y SACs with tailored Pt–O coordination numbers from ~3.4 to ~5. Specifically, the propylene selectivity significantly increased from 65.4% to 94.1% when the coordination number of Pt–O was increased from ~3.4 to ~5, however, the variation in the coordination number of Pt–O slightly influenced the turnover frequency (TOF) values. Density functional theory (DFT) calculations on the reaction paths depicted that Pt single atom on Fe_2O_3 tended to selectively catalyze propyne to propylene, while Pt single atom on FeOOH favored propyne over-hydrogenation (POH), being well consistent with our experimental observations.

Results and Discussion

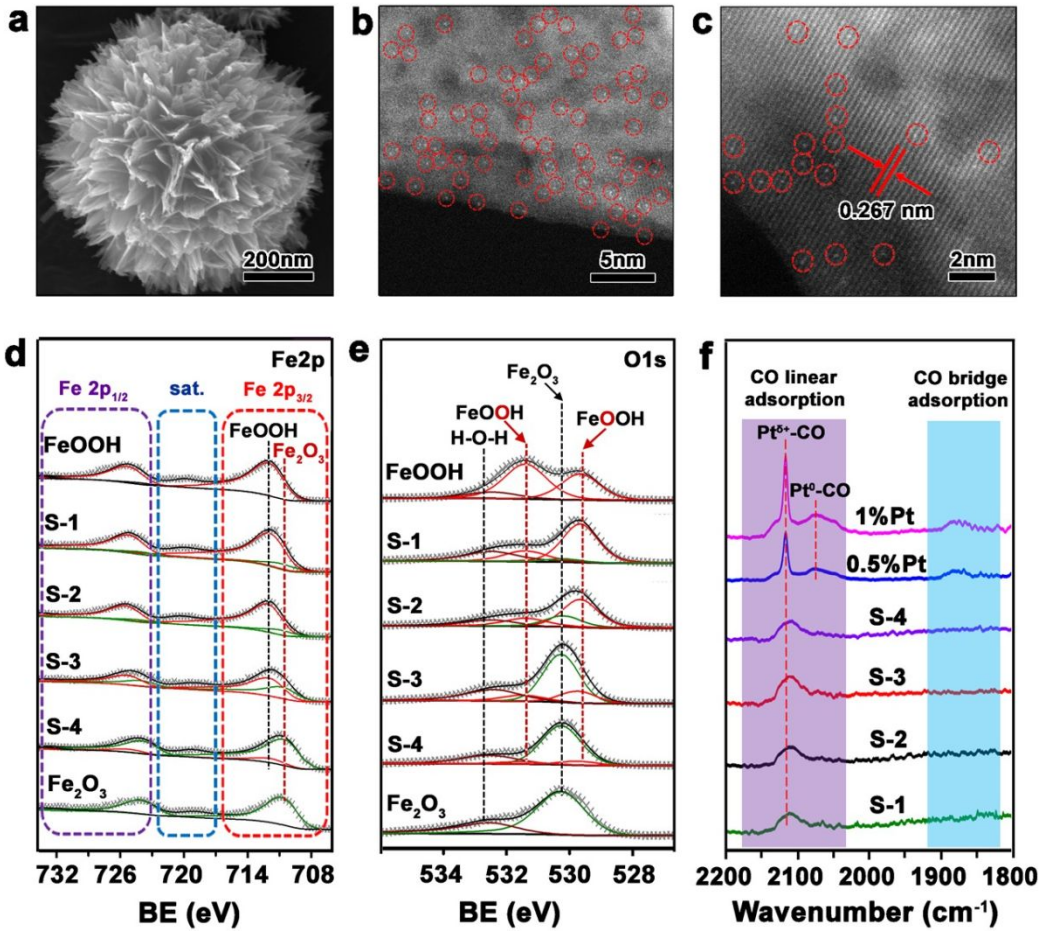

Figure 1. Structural analysis of different catalysts. (a) SEM image of S-4, (b) AC-STEM image of S-4. The isolated Pt atoms are labeled with red cycles, (c) high resolution AC-STEM image of S-4, (d) Fe 2p XPS spectra of FeOOH and Pt/FeO_xH_y catalysts, (e) O 1s XPS spectra of FeOOH and Pt/FeO_xH_y catalysts, (f) CO-DRIFTS spectra of Pt/FeO_xH_y SACs, 0.5%Pt-FeO_xH_y and 1%Pt-FeO_xH_y. The CO linear and bridge adsorption are highlighted in purple and blue in (f). Note that the absence of CO bridge adsorption peak in the CO-DRIFTS spectra suggests Pt atoms are presented as single state in Pt/FeO_xH_y SACs, while the presence of CO bridge adsorption and linear adsorption in the CO-DRIFTS spectra of 0.5%Pt-FeO_xH_y and 1%Pt-FeO_xH_y suggests Pt atoms were presented as cluster or nanoparticle.

FeOOH was prepared via a simple hydrothermal process, and Pt/FeO_xH_y SACs were prepared by depositing a certain amount of $Pt(NH_3)(NO_3)_2$ on FeOOH (see experimental section). Urchin-like structure with an average size of ~1 μm was successfully prepared (Figure S1a). After depositing Pt, no obvious change in morphology or size of FeOOH nanostructures was observed (Figures 1b, 1c, and S1c). More importantly, the urchin-like shape was maintained even when the thermal treatment temperature was increased to 400 ^{o}C (Figure S1d−f). These calcinated samples at 160, 200, 300, and 400 ^{o}C were simplified as S-1, S-2, S-3, and S-4, respectively. X-ray diffraction (XRD) patterns indicated that FeOOH gradually evolved into Fe_2O_3 with the increased treatment temperature. For instance, characteristic peaks of α-FeOOH (PCPDF No.: 81-0463) appeared in the XRD pattern of S-1, while intense peaks of α-Fe_2O_3 (PCPDF No.: 79-0007) were observed in the XRD pattern of S-4 (Figure S2). No peaks corresponding to Pt appeared in the XRD patterns of Pt/FeO_xH_y SACs, which might be attributed to the low loading amount and high dispersity of Pt in SACs. Moreover, aberration-corrected STEM (AC-STEM) measurement was employed to characterize the isolated state of Pt atoms in Pt/FeO_xH_y SACs. We took S-4 as an example. Pt single atom was observed in the AC-STEM image (red dash cycles in Figures 1b and S3), suggesting that Pt atoms were presented as single state. The lattice distance of 0.267 nm corresponded to α-Fe_2O_3 (104) facet (Figure 1c). In contrast, Pt clusters with a mean size of ~1.2 and ~1.9 nm were observed in the AC-STEM image of 0.5%Pt-FeO_xH_y and 1%Pt-FeO_xH_y, respectively (Figures S4 and S5).

X-ray photoelectron spectroscopy (XPS) measurement was performed to study the surface properties of those samples. As depicted in Figure 1d, the characteristic peaks at 712.3, 725.1, and 719.2 eV in the XPS spectrum of FeOOH were indexed as Fe $2p_{3/2}$, Fe $2p_{1/2}$, and Fe satellite, respectively.[42,43] The peaks of Fe $2p_{3/2}$ and Fe $2p_{1/2}$ appeared at 710.7 and 723.8 eV in the XPS

spectrum of Fe_2O_3 (Figure 1d).[42,43] For Pt/FeO_xH_y SACs, Fe was a mixture of FeOOH and Fe_2O_3, and the molar ratio of Fe_2O_3 gradually increased from 9.1% to 91.3% with the increased temperature from 160 to 400 °C (Table S1). Similarly, O 1s XPS spectra indicated that Pt/FeO_xH_y consisted of FeOOH and Fe_2O_3, in which the peaks at 529.5, 530.2, 531.4, and 532.6 eV corresponded to O−Fe in FeOOH, O−Fe in Fe_2O_3, O−H in FeOOH, and O−H in H_2O, respectively, (Figure 1e).[42] The absence of Pt peaks in XPS spectra might be attributed to the high dispersity and low content of Pt in Pt/FeO_xH_y SACs (Table S2). N_2 adsorption-desorption measurement indicated that the dehydration of FeOOH ($2FeOOH \rightarrow Fe_2O_3 + H_2O$) would result in the formation of porous structures (Figure S6 and Table S2). For instance, the surface area of FeOOH was 27.32 m^2/g, which significantly increased to 181.62 m^2/g in S-4. To further study the dehydration of FeOOH, thermogravimetric analysis (TGA) measurement was performed in both air and argon in the temperature range of 30−1000 °C. Both the TGA curves obtained in air and argon displayed similar features, suggesting that the weight loss during heating was caused by dehydration (Figure S7). Specifically, the weight loss at the temperature ranges of <150 °C and 150−800 °C were ascribed to the removal of adsorbed H_2O and FeOOH dehydration, respectively. Considering the fact that the highest treatment temperature for Pt/FeO_xH_y SACs was 400 °C, we concluded that FeOOH was partially dehydrated in Pt/FeO_xH_y SACs, which further confirmed the results from XPS measurement.

To further reveal the structures of Pt atoms, the diffuse reflectance infrared Fourier transform spectroscopy (DRIFTS) measurement was performed on different samples using CO as the prober molecule. A broad peak at 2070−2150 cm^{-1} was observed in the CO-DRIFTS spectra of Pt/FeO_xH_y SACs, which was indexed as the linear adsorption of CO on Pt atoms (Figure 1f).[44-46] In contrast, several peaks appeared at 2070−2150, 2020−2100, and 1850−1900 cm^{-1} in the CO-DRIFTS

spectra of 0.5%Pt-FeO_xH_y and 1%Pt-FeO_xH_y, which were ascribed to CO linear adsorption on $Pt^{\delta+}$, CO linear adsorption on Pt^0, and CO bridge adsorption on Pt, respectively.[44-47] Only the presence of CO linear adsorption in the CO-DRIFTS spectra of Pt/FeO_xH_y SACs confirmed the single state of Pt atoms in Pt/FeO_xH_y SACs, while the co-existence of CO linear and bridge adsorption in the CO-DRIFTS spectra of 0.5%Pt-FeO_xH_y and 1%Pt-FeO_xH_y suggested that Pt atoms were presented as small nanoparticles (Figure 1f).

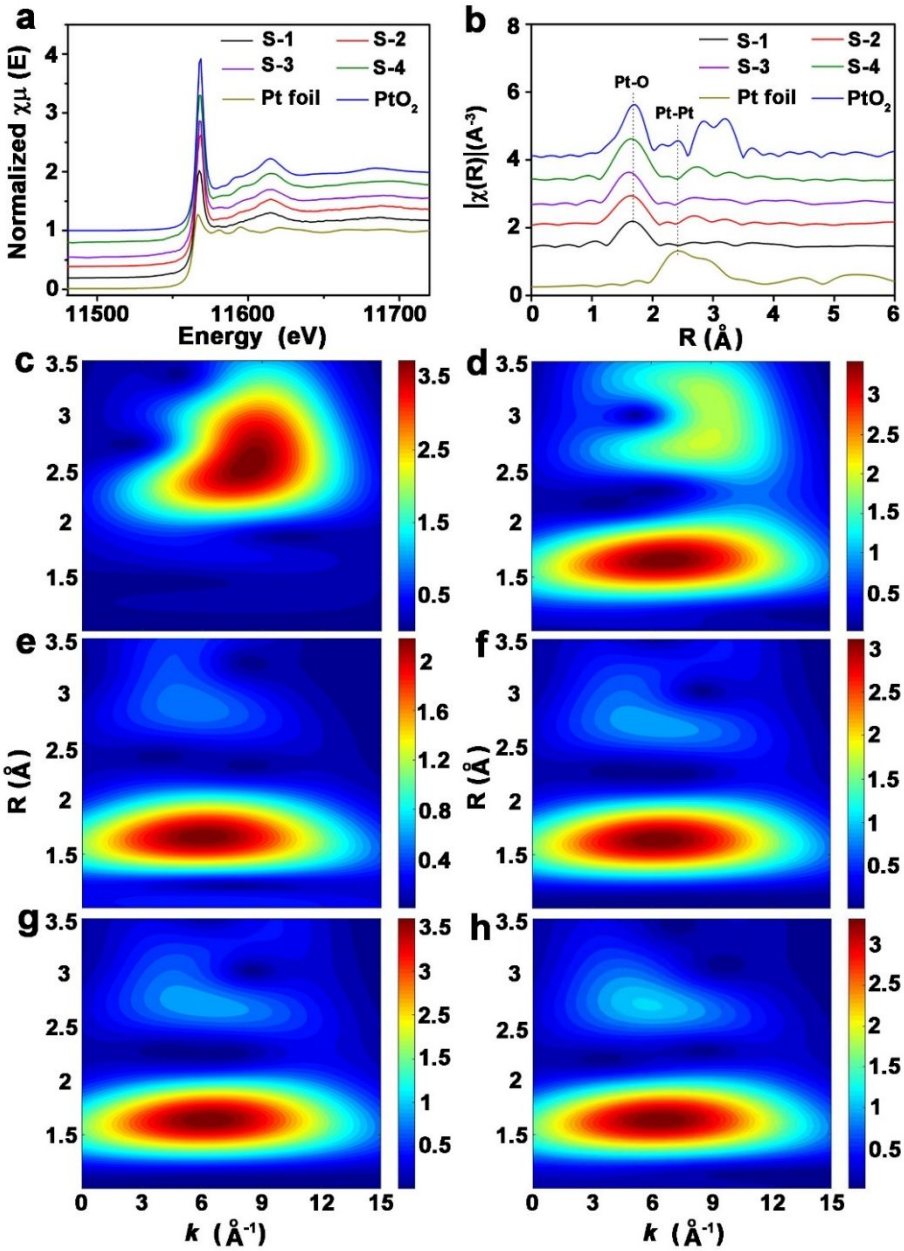

Figure 2. Structural analysis of Pt/FeO_xH_y SACs. (A) XANES spectra of Pt/FeO_xH_y SACs, Pt foil and PtO_2 at Pt L_3-edge. (B) EXAFS spectra of Pt/FeO_xH_y SACs, Pt foil and PtO_2 at Pt L_3-edge. Wavelet transform of EXAFS spectra at Pt L_3-edge, (C) Pt foil, (D) PtO_2, (E) S-1, (F) S-2, (G) S-3, and (H) S-4.

Pt L_3-edge X-ray absorption near-edge spectroscopy (XANES) and extended X-ray fine structure (EXAFS) were measured to study the electronic structures and coordination states of Pt, and Pt foil and Fe_2O_3 were used as references. As shown in Figure 2, comparing with the XANES spectrum of Pt foil, Pt in Pt/FeO_xH_y SACs were presented as their oxidation state. However, the lower absorption energies and weaker "white line" intensities in comparison to PtO_2 suggested that Pt atoms in Pt/FeO_xH_y SACs were low-coordinated (Figure 2a). The appearance of Fe_2O_3 features in the Fe K-edge XANES spectra of different Pt/FeO_xH_y SACs confirmed the dehydration of FeOOH to Fe_2O_3 during thermal treatment (Figure S8). The characteristic peaks of Pt−O and Pt−Pt coordination were observed at 1.7 and 2.4 Å, respectively, in the EXAFS spectra of PtO_2 and Pt foil. Only the peak of Pt−O coordination at 1.6−1.7 Å was observed in the EXAFS spectra of Pt/FeO_xH_y SACs, which implied that Pt atoms were presented as isolated state (Figure 2b). Moreover, wavelet transform of EXAFS spectra at Pt L_3-edge further confirmed the isolated state of Pt atoms in Pt/FeO_xH_y SACs, as evidenced by the disappearance of Pt−Pt coordination in the profile (Figures 2c−h). We analyzed the coordination environment of Pt in Pt/FeO_xH_y SACs by fitting the EXAFS spectra, and the coordination numbers of Pt−O in S-1, S-2, S-3, and S-4 were ~3.43, ~4.35, ~4.75, and ~5.04, respectively (Table S3). The aforementioned results revealed that the coordination number of Pt single atom in Pt/FeO_xH_y SACs could be systematically tuned during synthetic process. As a comparison, XANES spectra of 0.5%Pt-FeO_xH_y and 1%Pt-FeO_xH_y at Pt L_3-edge were obtained. Pt in 0.5%Pt-FeO_xH_y and 1%Pt-

FeO_xH_y exhibited similar features to Pt foil in XANES spectra. However, the "white line" intensities of 0.5%Pt-FeO_xH_y and 1%Pt-FeO_xH_y were higher than that of Pt foil, which indicated that the surface of Pt nanoparticles was partially oxidized (Figure S9a). EXAFS spectra analysis further confirmed the partial oxidation nature of Pt nanoparticles (Figure S9b). Consequently, results from XANES and EXAFS spectra were consistent with those from AC-STEM images and CO-DRIFTS spectra (Figure 1), which vividly revealed the isolated state of Pt atoms in Pt/FeO_xH_y SACs.

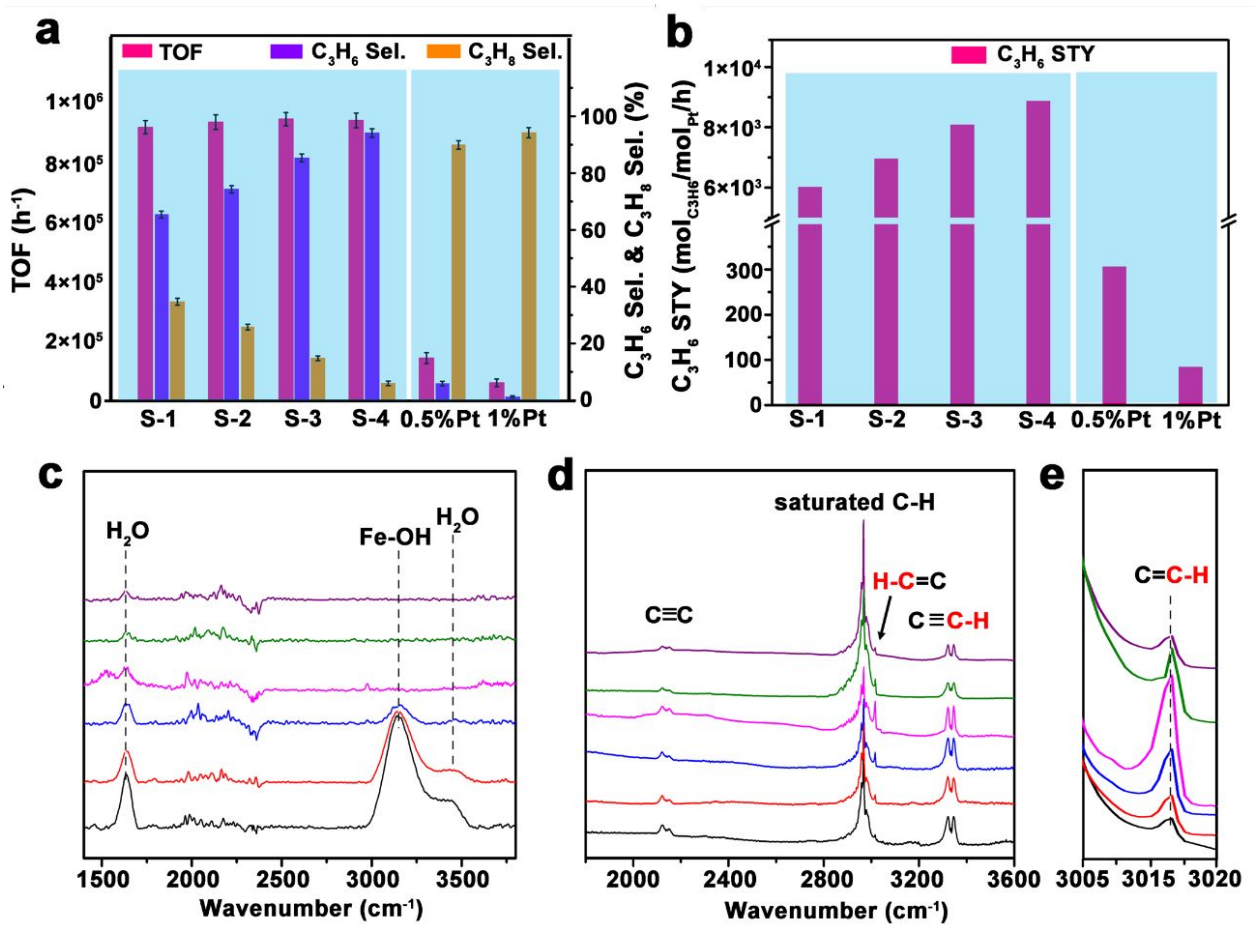

Figure 3. Catalytic performance of PSH on different catalysts. (A) The TOF values, C_3H_6 selectivity and C_3H_8 selectivity of different catalysts. (B) The C_3H_6 STY of different catalysts. The columns of Pt SACs and Pt nanoparticles are highlighted in blue and purple, respectively, in (A)

and (B). Reaction conditions: $C_3H_4/H_2/N_2$ = 3/30/2 mL/min, T = 120 °C, catalyst weight: 100 mg. (C) In-situ DRIFTS spectra of various catalysts in Ar. (D) In-situ DRIFTS spectra and (E) enlarged spectra in the range of 3005–3020 cm^{-1} of various catalysts in C_3H_4 and H_2. C_3H_4/H_2 = 1/10. Color in (C-E): black (S-1), red (S-1), blue (S-3), pink (S-4), green (0.5%Pt-FeO_xH_y), and purple (1%Pt-FeO_xH_y).

To further investigate the correlation of Pt−O coordination number and catalyst selectivity, Pt/FeO_xH_y SACs were used to catalyze PSH in a fix-bed reactor with an inner diameter of 10 mm.[48] As shown in Figure 3a, all Pt/FeO_xH_y SACs exhibited similar activities. When the coordination number of Pt−O was increased from ~3.43 to ~5.04, the turnover frequency (TOF) value slightly increased from 9.2×10^5 to 9.4×10^5 h^{-1}, whereas, the propylene selectivity significantly increased from 65.4% to 94.1%. Consequently, the propylene STY increased from 6.0×10^3 to 8.9×10^3 $mol_{C3H6}/mol_{Pt}/h$ (Figure 3b). In contrast, the TOF values of 0.5%Pt-FeO_xH_y and 1%Pt-FeO_xH_y were 3×10^5 and 1.4×10^5 h^{-1}, respectively, which were much lower than those of Pt/FeO_xH_y SACs (Figure 3a). Moreover, experimental results indicated that 0.5%Pt-FeO_xH_y and 1%Pt-FeO_xH_y favored POH), giving the propane selectivities of 89.8 and 94.1%, respectively. Consequently, the propylene STY of S-4 (8.9×10^3 $mol_{C3H6}/mol_{Pt}/h$) was ~28 and ~100 times higher than those of 0.5%Pt-FeO_xH_y (305.3 $mol_{C3H6}/mol_{Pt}/h$) and 1%Pt-FeO_xH_y (83.6 $mol_{C3H6}/mol_{Pt}/h$), respectively. These results indicated that Pt/FeO_xH_y SACs could be used as highly active and selective catalysts for PSH. In addition, *in situ* DRIFTS measurement was performed to monitor the surface species on catalysts. As shown in Figure 3c, when Ar was introduced into the cell (without C_3H_4 and H_2), intense peaks at 1641, 3151 and 3449 cm^{-1} were observed in the spectra of S-1, S-2, and S-3, which were ascribed to the H_2O bending vibration, stretching Fe-OH vibration, and H_2O stretching vibration, respectively,[49] in FeOOH (Figure 3c). FeOOH was gradually converted into Fe_2O_3 with

the increased treatment temperature, leading to the weakening peak intensity in the DRIFTS spectra (Figure 3c). When C_3H_4 and H_2 were introduced, the characteristic peaks of C_3H_4 at 2100−2200 and 3275−3390 cm^{-1} were observed (Figure 3d), which corresponded to the stretching vibration of C≡C and C−H associated with C≡C, respectively,[48] The shoulder peak at ~3015 cm^{-1} was indexed as the stretching vibration unsaturated C−H associated with C=C, indicating that propylene was formed (Figures 3d and 3e). More importantly, the intensity of propylene peak strongly varied in the DRIFTS spectra of different catalysts, suggesting the propylene selectivities of Pt/FeO_xH_y SACs were different (Figure 3e). The gradual increase in the propylene peak intensity at 3015 cm^{-1} in the DRIFTS spectra implied that the increase in treatment temperature favored PSH. For 0.5%Pt-FeO_xH_y and 1%Pt-FeO_xH_y Catalysts, the weak peak at 3015 cm^{-1} but intense peaks at 2900−2985 cm^{-1} suggested that most of propyne was converted into propane.[48] Moreover, the spent catalysts were characterized by XRD and XPS measurement. Compared to the XRD patterns of the fresh SACs, no obvious changes in the XRD patterns of the spent SACs, suggesting the excellent stability of catalyst under the indicated conditions (**Figure S10**). Additionally, XPS measurement indicated the ratios of FeOOH/Fe_2O_3 in the spent SACs were maintained in the spent catalysts comparing with the fresh catalysts (**Figure S11** and **Table S4**). Specially, the ratios of FeOOH/Fe_2O_3 in the fresh and spent S-4 were 91.3/8.7 and 91.4/8.6, respectively, which further confirmed the excellent stability of SACs under the indicated reaction conditions (**Table S4**). Based on the above-mentioned results, we concluded that Pt SACs could significantly promote the selective hydrogenation of propyne to propylene.

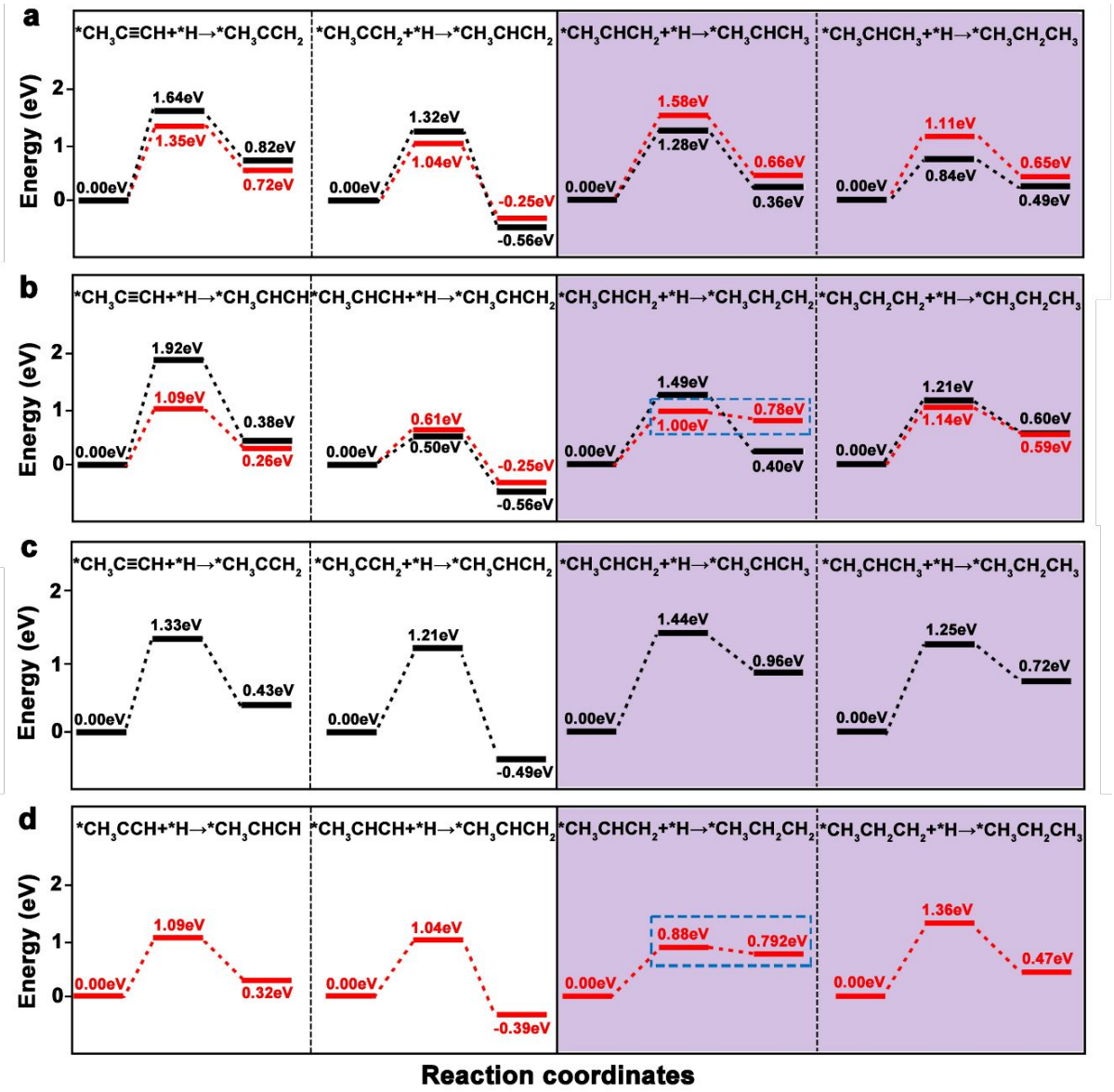

Figure 4. Energy profiles of propyne hydrogenation over Pt single atom on hydrogenated FeOOH and Fe_2O_3. (**a**) Energy profiles of propyne hydrogenation on 3-coordinated Pt single atom on hydrogenated FeOOH (black) and 7-coordinated Pt single atom on partially hydrogenated Fe_2O_3 (red) via C-1 path, (b) Energy profiles of propyne hydrogenation on 3-coordinated Pt single atom on hydrogenated FeOOH (black) and 7-coordinated Pt single atom on partially hydrogenated Fe_2O_3 (red) via C-2 path. (**c**) Energy profiles of propyne hydrogenation on 4-coordinated Pt single atom on partially hydrogenated Fe_2O_3 via C-1 path, (b) Energy profiles of propyne hydrogenation

on 4-coordinated Pt single atom on partially hydrogenated Fe_2O_3 via C-2 path. Note that the POH is highlighted in purple.

To further reveal the mechanism, DFT calculations were performed on Pt single atom supported on FeOOH and Fe_2O_3. DFT results implied that Pt single atom preferred to replace one surface H atom on FeOOH (110) surface and coordinate with two surface O atoms and one sublayer O atom, giving a coordination number of 3 (Figure S12). On Fe_2O_3 (001) surface, Pt single atom preferred to occupy the hollow sites of Fe_2O_3 (001) surface surrounded by six surface oxygen atoms, leading to a variable coordination number of 4 or 7 due to the structural relaxation (Figure S13). Taking into considerations that the PSH occurred in hydrogen-rich environment, O atoms on FeOOH and Fe_2O_3 surfaces should be terminated with H atoms. Therefore, the hydrogenated Pt/FeOOH and Pt/Fe_2O_3 surface were selected to mimic the surfaces. In Horiuti-Polanyi mechanism, the first H atom might be added to either the terminal carbon (C-1 path) or middle carbon atom (C-2 path) of propyne and propylene molecules, the energy barriers of different paths during propyne hydrogenation were calculated. Given that the structural relaxation of Pt single atom on Fe_2O_3 (001) surface, DFT calculations were performed on hydrogenated Pt/FeOOH (110) surface, 7-coordinated and 4-coordinated Pt single atom on partially hydrogenated Fe_2O_3 (001) surface, as depicted in Figure 4. The atomic structures of initial state, transition state and final state were given in Figures S14−19. For C-1 path, the energy barrier for the first step ($^*CH_3C{\equiv}CH + ^*H \rightarrow ^*CH_3CCH_2$) was 1.35 eV on Pt/$Fe_2O_3$ surface with a Pt−O coordination number of 7 (red profile), which was higher than that of C-2 path (1.09 eV, red profile in Figure 4b), suggesting that propyne hydrogenation to propylene preferred C-2 path on Pt/Fe_2O_3 surface. In contrast, propyne hydrogenation to propylene preferred C-1 path on Pt/FeOOH surface, because the energy barrier of C-1 path (1.64 eV, black profile in Figure 4a) was lower than that of

C-2 path (1.92 eV, black profile in Figure 4b). DFT calculations revealed that Pt/FeOOH favored POH comparing with Pt/Fe_2O_3. Typically, the energy barriers of $^*C_3H_7$ formation on Pt/FeOOH via C-1 and C-2 path were 1.28 eV (black profile in Figure 4a) and 1.49 eV (black profile in Figure 4b), respectively, indicating that POH competitively occurred via C-1 and C-2 path on Pt/FeOOH. Conversely, the energy barrier for the formation of $^*C_3H_7$ ($^*CH_3CHCH_2$+$^*H$→$^*CH_3CHCH_3$) on Pt/Fe_2O_3 via C-1 path was 1.58 eV (red profile in Figure 4A), which was higher than that via C-2 path (1.00 eV, red profile in Figure 4b), suggesting that C-2 path was more preferential on Pt/Fe_2O_3. Interestingly, the energy barrier of $^*C_3H_7$ dehydrogenation ($^*C_3H_7$→$^*CH_3CHCH_2$+$^*H$) was only 0.22 eV (highlighted by blue dash rectangle), which was much lower than that of $^*C_3H_7$ formation from propylene ($^*CH_3CHCH_2$+$^*H$→$^*CH_3CHCH_3$), indicating that the formation of $^*C_3H_7$ was thermodynamically suppressed on Pt/Fe_2O_3. In other words, $^*C_3H_7$ tended to dehydrogenize once it was formed on Pt/Fe_2O_3. Moreover, DFT calculations were performed on Fe_2O_3 (001) surface with a 4-coordianted Pt single atom. As shown in Figure 4c−d, similar phenomenon with 7-coordianted Pt single atom on Fe_2O_3 (001) surface were observed. The energy barrier of $^*C_3H_7$ dehydrogenation ($^*C_3H_7$→$^*CH_3CHCH_2$+$^*H$) was only 0.09 eV (highlighted by blue dash rectangle in Figure 4d), which was much lower than that of $^*C_3H_7$ formation from propylene (0.88 eV, Figure 4d). Note that Pt/FeOOH exhibited a much stronger propylene adsorption than Pt/Fe_2O_3 (2.11 *vs.* 1.33 eV), suggesting that $^*C_3H_7$ tended to dehydrogenize into $^*C_3H_6$ once it was formed on Pt/Fe_2O_3. Based on the aforementioned results from DFT calculations, we concluded that Pt/FeO_xH_y SACs with a higher Pt−O coordination number could selectively catalyze PSH to form propylene, while Pt/FeOOH with a lower Pt−O coordination number favored POH to form propane.

Conclusions

In conclusion, we synthesized a series of urchin-like FeO_xH_y nanostructures supported Pt SACs with tunable Pt−O coordination numbers via a simple thermal treatment. The removal of H and O atoms from FeOOH in the form of H_2O during thermal treatment resulted in a consecutive tunability of Pt−O coordination numbers from ~3.43 to ~5.04. The structures of Pt SACs were detailed revealed by AC-STEM, CO-DRIFTS, XANES, and EXAFS measurements. The increase in the Pt−O coordination numbers led to a significant increase in propylene selectivity but a negligible influence in activity during PSH. DFT calculations indicated that Pt SACs with high Pt−O coordination number favored PSH, while Pt SACs with low Pt−O coordination number favored POH. This study may deepen the understanding on coordination environment-catalytic performance correlation and also promote the fundamental researches in single atom catalysis.

ASSOCIATED CONTENT

Supporting Information. The Supporting Information is available free of charge on the ACS Publications website site.

Experimental section, Figures S1−S19, Tables S1−S4 (PDF).

Corresponding Author

*hplin@suda.edu.cn, qiaozhang@suda.edu.cn

Author Contributions

†These authors contributed equally to this work.

Notes

The authors declare no competing financial interests.

ACKNOWLEDGMENT

This work is supported by National Natural Science Foundation of China (51922073, 21673150, and 51802206) and Natural Science Foundation of Jiangsu Province (BK20180097, BK20180846). We acknowledge the financial support from the 111 Project, Collaborative Innovation Center of Suzhou Nano Science and Technology (NANO-CIC) and the Priority Academic Program Development of Jiangsu Higher Education Institutions (PAPD).

REFERENCES

(1) Zhang, L.; Zhou, M.; Wang, A.; Zhang, T. Selective hydrogenation over supported metal catalysts: from nanoparticles to single atoms. *Chem. Rev.* **2020**, *120*, 683−733.

(2) Wang, X.; Li, Z., Qu, Y.; Yuan, T.; Wang, W.; Wu, Y.; Li, Y. Review of metal catalysts for oxygen reduction reaction: from nanoscale engineering to atomic design. *Chem* **2019**, *5*, 1486-1511.

(3) Yang, X.; Wang, A.; Qiao, B.; Li, J.; Liu, J.; Zhang, T. Single-atom catalysts: a new frontier in heterogeneous catalysis. *Accounts Chem. Res.* **2013**, *46*, 1740−1748.

(4) Liu, L.; Corma, A. Metal catalysts for heterogeneous catalysis: from single atoms to nanoclusters and nanoparticles. *Chem. Rev.* **2018**, *118*, 4981−5079.

(5) Zhang, L., Ren, Y., Liu, W., Wang, A. and Zhang, T. Single-atom catalyst: a rising star for green synthesis of fine chemicals. *Natl. Sci. Rev.* **2018**, *5*, 653−672.

(6) Zheng, Y.; Qiao, S. Metal-organic framework assisted synthesis of single-atom catalysts for energy applications. *Natl. Sci. Rev.* **2018**, *5*, 626−627.

(7) Chen, Y.; Ji, S.; Chen, C.; Peng, Q.; Wang, D.; Li, Y. Single-atom catalysts: synthetic strategies and electrochemical applications. *Joule* **2018**, *2*, 1242−1264.

(8) Qiao, B.; Wang, A.; Yang, X.; Allard, L.; Jiang, Z.; Cui, Y.; Liu, J.; Li, J.; Zhang, T. Single-atom catalysis of CO oxidation using Pt_1/FeO_x. *Nat. Chem.* **2011**, *3*, 634−641.

(9) Jeong, H.; Kwon, O.; Kim, B.; Bae, J.; Shin, S.; Kim, H.; Kim, J.; Lee, H. Highly durable metal ensemble catalysts with full dispersion for automotive applications beyond single-atom catalysts. *Nat. Catal.* **2020**, *3*, 368-375.

(10) Hülsey, M.; Zhang, B., Ma, Z., Asakura, H., Do, D., Chen, W., Tanaka, T., Zhang, P.; Wu, Z.; Yan, N. In situ spectroscopy-guided engineering of rhodium single-atom catalysts for CO oxidation. *Nat. Commun.* **2019**, *10*, 1330.

(11) Lu, Y.; Wang, J.; Yu, L.; Kovarik, L.; Zhang, X.; Hoffman, A.; Gallo, A.; Bare, S.; Sokaras, D.; Kroll, T.; Dagle, V.; Xin, H.; Karim, A. Identification of the active complex for CO oxidation over single-atom Ir-on-$MgAl_2O_4$ catalysts. *Nat. Catal.* **2018**, *2*, 149−156.

(12) Daelman, N.; Capdevila-Cortada, M.; Lopez, N. Dynamic charge and oxidation state of Pt/CeO_2 single-atom catalysts. *Nat. Mater.* **2019**, *18*, 1215−1221.

(13) Cui, X.; Li, H.; Wang, Y.; Hu, Y.; Hua, L.; Li, H.; Han, X.; Liu, Q.; Yang, F., He, L.; Chen, X.; Li, Q.; Xiao, J.; Deng, D.; Bao, X. Room-temperature methane conversion by graphene-confined single iron atoms. *Chem* **2018**, *4*, 1902−1910.

(14) Bai, S.; Liu, F.; Huang, B.; Li, F.; Lin, H.; Wu, T.; Sun, M.; Wu, J.; Shao, Q.; Xu, Y.; Huang, X. High-efficiency direct methane conversion to oxygenates on a cerium dioxide nanowires supported rhodium single-atom catalyst. *Nat. Commun.* **2020**, *11*, 954.

(15) Shao, X.; Yang, X.; Xu, J.; Liu, S.; Miao, S.; Liu, X.; Su, X.; Duan, H.; Huang, Y.; Zhang, T. Iridium single-atom catalyst performing a quasi-homogeneous hydrogenation transformation of CO_2 to formate. *Chem* **2019**, *5*, 693−705.

(16) Millet, M.; Algara-Siller, G.; Wrabetz, S.; Mazheika, A.; Girgsdies, F.; Teschner, D.; Seitz, F.; Tarasov, A., Levchenko, S., Schlögl, R.; Frei, E. Ni single atom catalysts for CO_2 activation. *J. Am. Chem. Soc.* **2019**, *141*, 2451−2461.

(17) He, Q.; Liu, D.; Lee, J.; Liu, Y.; Xie, Z.; Hwang, S.; Kattel, S.; Song, L.; Chen, J. Electrochemical conversion of CO_2 to syngas with controllable CO/H_2 ratios over Co and Ni single-atom catalysts. *Angew. Chem. Int. Ed.* 2020, *59*, 3033−3037.

(18) Rong, X.; Wang, H.; Lu, X.; Si, R.; Lu, T. Controlled synthesis of a vacancy-defect single-atom catalyst for boosting CO_2 electroreduction. *Angew. Chem. Int. Ed.* **2020**, *59*, 1961−1965.

(19) Zhang, J.; Zhao, Y.; Guo, X.; Chen, C.; Dong, C.; Liu, R.; Han, C.; Li, Y.; Gogotsi, Y.; Wang, G. Single platinum atoms immobilized on an MXene as an efficient catalyst for the hydrogen evolution reaction. *Nat. Catal.* **2018**, *1*, 985–992.

(20) Cao, L.; Luo, Q.; Liu, W.; Lin, Y.; Liu, X.; Cao, Y.; Zhang, W.; Wu, Y.; Yang, J.; Yao, T.; Wei, S. Identification of single-atom active sites in carbon-based cobalt catalysts during electrocatalytic hydrogen evolution. *Nat. Catal.* **2018**, *2*, 134–141.

(21) Cheng, N.; Stambula, S.; Wang, D.; Banis, M.; Liu, J.; Riese, A.; Xiao, B.; Li, R.; Sham, T.; Liu, L.; Botton, G.; Sun, X. Platinum single-atom and cluster catalysis of the hydrogen evolution reaction. *Nat. Commun.* **2016**, *7*, 13638.

(22) Lin, J.; Wang, A.; Qiao, B.; Liu, X.; Yang, X.; Wang, X.; Liang, J.; Li, J.; Liu, J.; Zhang, T. Remarkable performance of Ir_1/FeO_x single-atom catalyst in water gas shift reaction. *J. Am. Chem. Soc.* **2013**, *135*, 15314–15317.

(23) Wei, H.; Liu, X.; Wang, A.; Zhang, L.; Qiao, B.; Yang, X.; Huang, Y.; Miao, S.; Liu, J.; Zhang, T. FeO_x-supported platinum single-atom and pseudo-single-atom catalysts for chemoselective hydrogenation of functionalized nitroarenes. *Nat. Commun.* **2014**, *5*, 5635.

(24) Yan, H.; Cheng, H.; Yi, H.; Lin, Y.; Yao, T.; Wang, C.; Li, J.; Wei, Q.; Lu, J. Single-atom Pd_1/graphene catalyst achieved by atomic layer deposition: remarkable performance in selective hydrogenation of 1,3-butadiene. *J. Am. Chem. Soc.* **2015**, *137*, 10484–10487.

(25) Gao, J.; Yang, H.; Huang, X.; Hung, S.; Cai, W.; Jia, C.; Miao, S.; Chen, H.; Yang, X.; Huang, Y.; Zhang, T.; Liu, B. Enabling direct H_2O_2 production in acidic media through rational design of transition metal single atom catalyst. *Chem* **2020**, *6*, 658–674.

(26) Feng, Q.; Zhao, S.; Xu, Q.; Chen, W.; Tian, S.; Wang, Y.; Yan, W.; Luo, J.; Wang, D.; Li, Y. Mesoporous nitrogen-doped carbon-nanosphere-supported isolated single-atom Pd catalyst for highly efficient semihydrogenation of acetylene. *Adv. Mater.* **2019**, *31*, 1901024.

(27) Yang, H.; Shang, L.; Zhang, Q.; Shi, R.; Waterhouse, G.; Gu, L.; Zhang, T. A universal ligand mediated method for large scale synthesis of transition metal single atom catalysts. *Nat. Commun.* **2019**, *10*, 4585.

(28) Sarma, B.; Kim, J.; Amsler, J.; Agostini, G.; Weidenthaler, C.; Pfänder, N.; Arenal, R.; Concepción, P.; Plessow, P.; Studt, F.; Prieto, G. One-pot cooperation of single-atom Rh and Ru solid catalysts for a selective tandem olefin isomerization-hydrosilylation process. *Angew. Chem. Int. Ed.* **2020**, *59*, 5806–5815.

(29) Zhang, Z.; Feng, C.; Liu, C.; Zuo, M.; Qin, L.; Yan, X.; Xing, Y.; Li, H.; Si, R.; Zhou, S.; Zeng, J. Electrochemical deposition as a universal route for fabricating single-atom catalysts. *Nat. Commun.* **2020**, *11*, 1215.

(30) Liu, Y.; Li, Z.; Yu, Q.; Chen, Y.; Chai, Z.; Zhao, G.; Liu, S.; Cheong, W.; Pan, Y.; Zhang, Q.; Gu, L.; Zheng, L.; Wang, Y.; Lu, Y.; Wang, D.; Chen, C.; Peng, Q.; Liu, Y.; Liu, L.; Chen, J.; Li, Y. A general strategy for fabricating isolated single metal atomic site catalysts in Y zeolite. *J. Am. Chem. Soc.* **2019**, *141*, 9305–9311.

(31) Wang, C.; Mao, S.; Wang, Z.; Chen, Y.; Yuan, W.; Ou, Y.; Zhang, H.; Gong, Y.; Wang, Y.; Mei, B.; Jiang, Z.; Wang, Y. Insight into single-atom-induced unconventional size dependence over CeO_2-supported Pt catalysts. Chem (2020, *6*, 752–765.

(32) Zhang, J.; Zhao, Y.; Guo, X.; Chen, C.; Dong, C.; Liu, R.; Han, C.; Li, Y.; Gogoysi, Y.; Wang, G. Single platinum atoms immobilized on an MXene as an efficient catalyst for the hydrogen evolution reaction. *Nat. Catal.* **2018**, *1*, 985–992.

(33) Zhu, Y.; Sun, W.; Luo, J.; Chen, W.; Cao, T.; Zheng, L.; Dong, J.; Zhang, J.; Zhang, M.; Han, Y.; Chen, C.; Peng, Q.; Wang, D.; Li, Y. A cocoon silk chemistry strategy to ultrathin N-doped carbon nanosheet with metal single-site catalysts. *Nat. Commun.* **2018**, *9*, 3861.

(34) Wei, S.; Li, A.; Liu, J.; Li, Z.; Chen, W.; Gong, Y.; Zhang, Q.; Cheong, W.; Wang, Y.; Zheng, L.; Xiao, H.; Chen, C.; Wang, D.; Peng, Q.; Gu, L.; Han, X.; Li, J.; Li, Y. Direct observation of noble metal nanoparticles transforming to thermally stable single atoms. *Nat. Nanotechnol.* **2018**, *13*, 856–861.

(35) Geng, Z.; Cao, Y.; Chen, W.; Kong, X.; Liu, Y.; Yao, T.; Lin, Y. Regulating the coordination environment of Co single atoms for achieving efficient electrocatalytic activity in CO_2 reduction. *Appl. Catal. B: Environ.* **2018**, *240*, 234–240.

(36) Gong, Y.; Jiao, L.; Qian, Y.; Pan, C.; Zheng, L.; Cai, X.; Liu, B.; Yu, S.; Jiang, H. Regulating the coordination environment of MOF-templated single-atom nickel electrocatalysts for boosting CO_2 reduction. *Angew. Chem. Int. Ed.* **2020**, *59*, 2705–2709.

(37) Fei, H.; Dong, J.; Feng, Y.; Allen, C.; Wan, C.; Volosskiy, B.; Li, M.; Zhao, Z.; Wang, Y.; Sun, H.; An, P.; Chen, W., Guo, Z., Lee, C., Chen, D. Shakir, I. Liu, M., Hu, T., Li, Y.; Kirkland, A.; Duan, X.; Huang, Y. General synthesis and definitive structural identification of MN_4C_4 single-atom catalysts with tunable electrocatalytic activities. *Nat. Catal.* **2018**, *1*, 63–72.

(38) Zhang, J.; Zhao, Y.; Chen, C.; Huang, Y.; Dong, C.; Chen, C.; Liu, R.; Wang, C.; Yan, K.; Li, Y.; Wang, G. Tuning the coordination environment in single-atom catalysts to achieve highly efficient oxygen reduction reactions. *J. Am. Chem. Soc.* **2019**, *141*, 20118–20126.

(39) Jakub, Z.; Hulva, J.; Meier, M.; Bilem, R.; Kraushofer, F.; Setvin, M.; Schmid, M.; Diebold, U.; Franchini, C.; Parkinson, G. Local structure and coordination define adsorption in a model Ir_1/Fe_3O_4 single-atom catalyst. *Angew. Chem. Int. Ed.* **2019**, *131*, 14099–14106.

(40) Wang, X.; Chen, Z.; Zhao, X.; Yao, T.; Chen, W.; You, R.; Zhao, C.; Wu, G.; Wang, J.; Huang, W.; Yang, J.; Hong, X.; Wei, S.; Wu, Y.; Li, Y. Regulation of coordination number over single Co sites: triggering the efficient electroreduction of CO_2. *Angew. Chem. Int. Ed.* **2018**, *57*, 1944–1948.

(41) Ren, Y.; Tang, Y.; Zhang, L.; Liu, X.; Li, L.; Miao, S.; Su, D.; Wang, A.; Li, J.; Zhang, T. Unraveling the coordination structure-performance relationship in Pt_1/Fe_2O_3 single-atom catalyst. *Nat. Commun.* **2019**, *10*, 4500.

(42) Owusu, K.; Qu, L.; Li, J.; Wang, Z.; Zhao, K.; Yang, C.; Hercule, K.; Lin, C.; Shi, C.; Wei, Q.; Zhou, L.; Mai, L. Low-crystalline iron oxide hydroxide nanoparticle anode for high-performance supercapacitors. *Nat. Commun.* **2017**, *8*, 14264.

(43) Ma, B.; Tong, X.; Guo, C.; Guo, X.; Guo, X.; Keil, F. Pyrite nanoparticles: an earth-abundant mineral catalyst for activation of molecular hydrogen and hydrogenation of nitroaromatics. *RSC Adv.* **2016**, *6*, 55220–55224.

(44) Ding, K.; Gulec, A.; Johnson, A.; Schweitzer, N.; Stucky, G.; Marks, L.; Stair, P. Identification of active sites in CO oxidation and water-gas shift over supported Pt catalysts. *Science* 2015, *350*, 189–192.

(45) Borchert, H.; Fenske, D.; Kolny-Olesiak, J.; Parisi, J.; Al-Shamery, K.; Bäumer, M. Ligand-capped Pt nanocrystals as oxide-supported catalysts: FTIR spectroscopic investigations of the adsorption and oxidation of CO. *Angew. Chem. Int. Ed.* **2007**, *46*, 2923–2926.

(46) Kale, M.; Christopher, P. Utilizing quantitative in situ FTIR spectroscopy to identify well-coordinated Pt atoms as the active site for CO oxidation on Al_2O_3-supported Pt catalysts. *ACS Catal.* **2016**, *6*, 5599–5609.

(47) Zhang, Z.; Zhu, Y.; Asakura, H.; Zhang, B.; Zhang, J.; Zhou, M.; Han, Y.; Tanaka, T.; Wang, A.; Zhang, T.; Yan, N. Thermally stable single atom Pt/m-Al_2O_3 for selective hydrogenation and CO oxidation. *Nat. Commun.* **2017**, *8*, 16100.

(48) Xu, Y.; Bian, W.; Pan, Q.; Chu, M.; Cao, M.; Li, Y.; Gong, Z.; Wang, R.; Cui, Y.; Lin, H.; Zhang, Q. Revealing the active sites of Pd nanocrystals for propyne semihydrogenation: from theory to experiment. *ACS Catal.* **2019**, *9*, 8471–8480.

(49) Yang, H.; Zhang, S.; Cao, R.; Deng, X.; Li, Z.; Xu, J. (Constructing the novel ultrafine amorphous iron oxyhydroxide/g-C_3N_4 nanosheets heterojunctions for highly improved photocatalytic peroformance. *Sci. Rep*. **2017**, *7*, 8686.

TOC